Controlling chaos experimentally in systems exhibiting large effective Lyapunov exponents

B. Hübinger, R. Doerner, and W. Martienssen

Physikalisches Institut der J.W. Goethe-Universität,
Robert-Mayer-Strasse 2-4, D-60325 Frankfurt am Main, Germany

M. Herdering, R. Pitka,* and U. Dressler

Daimler-Benz AG, Research Institute Frankfurt, Goldsteinstrasse 235, D-60528 Frankfurt, Germany

We investigate experimentally the performance of the Ott, Grebogi, and Yorke [Phys. Rev. Lett. **64**, 116 (1989)] feedback concept to control chaotic motion. The experimental systems are a driven pendulum and a driven bronze ribbon. Both setups have unstable periodic orbits characterized by large effective Lyapunov exponents. All control vectors for the feedback control are extracted from the experimental data. To do this for the pendulum a global model obtained by the flow field analysis of Cremers and Hübler [Z. Naturforsch. Teil A **42**, 797 (1987)] is used, and for the bronze ribbon linear approximations in embedding space are exploited. We analyze the problems that arise due to the amplification of noise by large effective Lyapunov exponents in the determination of the control values as well as in the performance of the experimental control. Successful control can be achieved in our experiments by applying the "local control method" which allows a quasicontinuous adjustment of the control parameter in contrast to adjusting the control parameter only once per return time of the Poincaré map.

PACS number(s): 05.45.+b

INTRODUCTION

Since the late 1970s, nonlinear dynamics has attracted the interest of an increasing number of physicists, and powerful mathematical tools have been developed to analyze systems whose dynamics are governed by a low dimensional chaotic attractor. The reconstruction of the attractor even from measurements of only a single scalar variable and the successive determination of its ergodic properties, like fractal dimension, entropies, and Lyapunov exponents might be regarded as state of the art available to many experimentalists nowadays.

Having obtained a deep understanding of low dimensional chaos and appropriate diagnostic tools at hand many nonlinear dynamicists are now interested to use their skills in order to exploit chaos and nonlinearities. One of the most prominent activities to go beyond a sole description of chaotic behavior is the field of controlling chaos. The idea to influence a system in a desired prescribed way was first stated by Lüscher and Hübler. In Ref. [1] they propose an open loop control. They drive a system to a desired motion by adding a specially designed continuous, generally aperiodic driving force which has to be calculated in advance using a global model of the system.

A different approach is the feedback control of Ott, Grebogi, and Yorke (OGY) [2]. They proposed to control a chaotic motion by stabilizing one of the many unstable periodic orbits (UPO's) embedded in a chaotic attractor by only minor time-dependent parameter perturbations. This idea has triggered immense research activities to apply feedback control to chaotic systems. A survey of these activities can be found in the review article of Shinbrot *et al.* [3]. In what follows we concentrate on the feedback control ansatz of OGY.

The OGY-control approach is marked by a number of special features. First of all, the stabilization of an UPO is obtained by only tiny parameter perturbations because one forces the system to a motion which is already inherent in its dynamics. Second, there is typically a large number of different UPO's, even with low period, embedded in a strange attractor, allowing a great variability in the choice of the desired mode of the system. Different modes can be achieved within one and the same system by only small alterations in the feedback control without changing the overall parameter regime. Third, with respect to applications the most important feature of OGY's control method is that it does not require a global model of the system. Only knowledge of the system dynamics in the vicinity of the unstable orbit has to be available. As was emphasized in Ref. [2], the local dynamics including the determination of the UPO's itself can be obtained from a single data series using the well-known embedding technique. This feature opens up a wide-spread field of real world applications. Note that the exclusive use of time delay coordinates can give rise to more complicated control formulas as was discussed in [4–6].

Two classes of experimental realizations of the OGY

---

*Permanent address: Fachhochschule Frankfurt, Kleiststrasse 3, 60318 Frankfurt, Germany.

control have been reported so far. In the first [7–11], the measured data are analyzed on a computer and the control values are obtained from this analysis. After that the control is applied to the experimental system. To this class belongs the first demonstration of a successful control using OGY's method done by Ditto et al. [7]. All control values of their experiment, a gravitationally buckled magnetostrictive ribbon driven by a magnetic field, could be determined from an almost one-dimensional return map which is shown to describe the highly dissipative system. They apply the control once per return time which means around once per second. Other authors report on frequencies of control for this class of experiments typically in the range of 1 Hz [8] up to 100 Hz [9].

In the second class [12–17] the control coefficients are determined while running the experiment by observing in an analog feedback loop for which control values the systems stabilizes to formerly unstable solutions. This was introduced in an experiment (a diode resonator) by Hunt [12] and is called occasional proportional feedback (OPF). This strategy can be most effective in experiments whose internal frequency or driving frequency is so high that a computer assisted evaluation of the control coefficients becomes very difficult if not impossible. In these experiments the driving frequency (except that of [14]) is of the order of kHz.

In this paper, we focus on the first class of control concepts where the experimental data are analyzed on a computer to obtain optimal control values for the feedback control. We investigate how well the control values can be determined from noisy experimental data and we examine how noise affects the performance of the feedback control and what can be done in order to gain control in the presence of noise.

In order to investigate these questions we use two experimental systems. These are a driven pendulum and a horizontally vibrating bronze beam driven by an external magnetic field. Both systems have features which make them especially suitable to study different aspects of the OGY-control approach. First, they cannot be described by a one-dimensional return map. So one has to work with the full two-dimensional Poincaré mapping in order to calculate the control vectors from a global dynamical model of the system or from local fits around recurrent points. Second it turns out that both systems have UPO's which are highly unstable as can be seen from their unstable eigenvalues and their effective Lyapunov exponents.

The effective Lyapunov exponent $\lambda_{eff}(\mathbf{z}_F, T)$ (for the return time T) of an UPO $\mathbf{z}_F$ in one Poincaré section is related to the largest singular value (i.e., the maximal possible stretching rate) $\mu(\mathbf{z}_F, T)$ of the linearization $D_{\mathbf{z}_F}\phi^T = D_{\mathbf{z}_F}\mathbf{P}$ around $\mathbf{z}_F$ of the Poincaré map $\mathbf{P}$. $\lambda_{eff}(\mathbf{z}_F, T)$ is defined as [19]

$$\lambda_{eff}(\mathbf{z}_F, T) := \frac{1}{T}\ln\mu(\mathbf{z}_F, T). \qquad (1)$$

In contrast to the eigenvalues of an UPO its singular values and thus its effective Lyapunov exponents does depend on the chosen Poincaré section. As the effective Lyapunov exponents affect the predictability of a

future state [19] the large effective Lyapunov exponents of the UPO's found in our experiments have severe consequences for the determination of the control values as well as for the performance of the feedback control itself.

Concerning the control performance of the feedback control it was already pointed out in [8] that the amplification of noise by large effective Lyapunov exponents can spoil the feedback control when the control parameter is adjusted only once per return time T of the Poincaré map. The reason for this is that an error ϵ in determining the actual state near a fixed point $\mathbf{z}_F$ in the Poincaré section can be amplified in the worst case during one return time T by $\mu(\mathbf{z}_F, T) = \exp[\lambda_{eff}(\mathbf{z}_F, T)T]$. If the amplified measurement error exceeds the size of OGY's control parallelogram [2] which is determined by the maximal allowed parameter perturbation, the feedback control fails. Thus for systems with large effective Lyapunov exponents one cannot wait one period to adjust the control parameter.

To overcome this problem, independently two similar extensions of the original OGY method have been developed. One is the *minimal expected deviation method* published by Reyl et al. [9]. It employs a different control condition than OGY which is obtained by requiring that the expected deviation of the trajectory from the desired orbit is minimized by the special choice of the control parameter. This scheme has been used to control an NMR laser. The other method, announced by Hübinger et al. [8] as *local control method*, will be extensively discussed in this paper. It allows a quasicontinuous application of the feedback in order to stabilize the UPO. Furthermore not only period one orbits but orbits of any period including aperiodic chaotic orbits can be stabilized.

The paper is organized as follows. In Sec. I we recall the original OGY control and we introduce our local controlling extension. In Sec. II the experimental setups of both experiments are described. In Sec. III the determination of the control vectors from experimental data is investigated and the influence of noise to this analysis is discussed. Furthermore, we propose a method to obtain the linearization of the Poincaré mapping around an UPO in the case of large effective Lyapunov exponents. Finally, in Sec. IV we successfully apply the local feedback control to the experiments using the control values obtained analyzing the measurement data. We summarize our results in Sec. V.

I. THE OGY CONTROL SCHEME

As in the experiments only two-dimensional Poincaré sections have been used we restrict the description of the original OGY control and of the local control to the case of three-dimensional continuous systems with two-dimensional Poincaré sections Σ. Extensions to higher dimensional systems may be found in Refs. [20–22]. For both methods we denote the accessible control parameter by p which can be varied with maximal possible perturbation δp_{max} around some value p_0.

A. The OGY control method

To stabilize an unstable periodic orbit lying in a chaotic attractor for $p = p_0$, Ott *et al.* [2] propose to monitor the system in a Poincaré section Σ. Whenever the intersection $\mathbf{z}_n$ of the orbit with the Poincaré section gets close enough to the UPO $\mathbf{z}_F(p_0) = \mathbf{P}(\mathbf{z}_F(p_0), p_0) \in \Sigma$ the control parameter p is adjusted to a new value p_n such that the next intersection $\mathbf{z}_{n+1}$, given by $\mathbf{z}_{n+1} = \mathbf{P}(\mathbf{z}_n, p_n)$, falls on the local stable manifold of $\mathbf{z}_F(p_0)$.

To calculate the necessary parameter perturbation δp_n one uses the linear approximation of the Poincaré map $\mathbf{P}$, near $\mathbf{z}_F(p_0)$ and p_0

$$\delta\mathbf{z}_{n+1} \cong A(p_0)\delta\mathbf{z}_n + \mathbf{w}\delta p_n, \qquad \delta\mathbf{z}_n \in \mathbb{R}^2 , \qquad (2)$$

with $\delta\mathbf{z}_n = \mathbf{z}_n - \mathbf{z}_F(p_0)$, $\delta p_n = p_n - p_0$, and $A(p_0) = D_{\mathbf{z}}\mathbf{P}(\mathbf{z}_F(p_0), p_0)$. The vector $\mathbf{w} = \frac{\partial \mathbf{P}}{\partial p}(\mathbf{z}_F, p_0)$ measures the sensitivity of the system to parameter perturbations.

An alternative way to describe the effect of the parameter perturbation δp is to look at the resulting shift of the fixed point

$$\mathbf{z}_F(p_0 + \delta p) - \mathbf{z}_F(p_0) \cong \mathbf{g}\delta p \qquad (3)$$

with $\mathbf{g} = \frac{\partial \mathbf{z}_F(p)}{\partial p}$.

Using this notation and linearizing $\mathbf{P}$ around $\mathbf{z}_F(p_n)$ the dynamics near $\mathbf{z}_F(p_0)$ can alternatively be described as

$$\delta\mathbf{z}_{n+1} = \mathbf{g}\delta p_n + A(p_n)(\delta\mathbf{z}_n - \mathbf{g}\delta p_n), \qquad (4)$$

with $A(p_n) = D_{\mathbf{z}}\mathbf{P}(\mathbf{z}_F(p_n), p_n)$.

Denoting with $\mathbf{f}_u$ the contravariant unstable eigenvector of $A(p_0)$ (i.e., $\mathbf{f}_u \cdot \mathbf{e}_s = 0$ and $\mathbf{e}_s$ being the stable eigendirection) and with λ_u the unstable eigenvalue the control requirement ($\mathbf{z}_{n+1}$ shall fall on the stable direction) can be expressed as $\mathbf{f}_u \cdot \delta\mathbf{z}_{n+1} = 0$. Together with (2) or (4) this renders the equivalent control formulas

$$\delta p_n = -\frac{\lambda_u}{\mathbf{f}_u \cdot \mathbf{w}}\mathbf{f}_u \cdot \delta\mathbf{z}_n \qquad (5)$$

or

$$\delta p_n = \frac{\lambda_u}{(\lambda_u - 1)\,\mathbf{f}_u \cdot \mathbf{g}}\mathbf{f}_u \cdot \delta\mathbf{z}_n \qquad (6)$$

assuming $A(p_0) \cong A(p_n)$. With this assumption the vectors $\mathbf{g}$ and $\mathbf{w}$ are related by

$$\mathbf{w} = (1 - A)\,\mathbf{g}. \qquad (7)$$

Note that with Eq. (2) the dynamics of the system in the vicinity of a periodic orbit is described by a linear mapping. Being at this point of the analysis the pole placement technique which is well known to the control engineering community can also be used to calculate a feedback control formula [20].

B. Local control method

In order to use N control stations per period T of the UPO one introduces N successive Poincaré sections $\Sigma_n, n = 0, \ldots, (N-1)$. Let $\mathbf{z}_F^n \in \Sigma_n$ be the intersections of the UPO with Σ_n and $\mathbf{P}^{(n,n+1)}$ be the mapping from one Poincaré section Σ_n to the next one Σ_{n+1}, i.e.,

$$\mathbf{z}^{n+1} = \mathbf{P}^{(n,n+1)}(\mathbf{z}^n, p^n), \qquad \mathbf{z}^n \in \Sigma_n \approx \mathbb{R}^2. \qquad (8)$$

Taking the natural (i.e., stroboscopic) Poincaré sections for a driven system the mapping $\mathbf{P}^{(n,n+1)}$ is just given by $\mathbf{P}^{(n,n+1)} = \phi_{|\Sigma_n}^{\Delta t}$, $\Delta t = T/N$, in the case of N equally spaced Poincaré sections Σ_n. Thus for large N the mappings $\mathbf{P}^{(n,n+1)}$ describe only short time evolutions of the system. We therefore call $\mathbf{P}^{(n,n+1)}$ the (time) local Poincaré mappings.

As in the preceding section one uses the linear approximation of $\mathbf{P}^{(n,n+1)}$ around $\mathbf{z}_F^n$ and p_0 given by

$$\delta\mathbf{z}^{n+1} = A^n\delta\mathbf{z}^n + \mathbf{w}^n\delta p^n , \qquad \delta\mathbf{z}^n = \mathbf{z}^n - \mathbf{z}_F^n \in \Sigma_n . \qquad (9)$$

with

$$A^n = D_{\mathbf{z}^n}\mathbf{P}^{(n,n+1)}(\mathbf{z}_F^n, p_0)$$

and

$$\mathbf{w}^n = \frac{\partial \mathbf{P}^{(n,n+1)}}{\delta p^n}(\mathbf{z}_F^n, p_0) .$$

For a periodic orbit $A^n, \mathbf{P}^{(n,n+1)}$ and $\mathbf{w}^n$ depend on n, only by n modulo N.

While in two dimensions the linearization $A = D_{\mathbf{z}_F}\mathbf{P}$ of the global Poincaré mapping $\mathbf{P}$ around an UPO lying in an attractor does only have real eigenvalues the linearization A^n of the mappings $\mathbf{P}^{(n,n+1)}$ can have complex eigenvalues. To establish a control formula we use the well-known fact that the linear mapping A^n deforms a ball around $\mathbf{z}_F^n$ into an ellipsoid around $\mathbf{z}_F^{n+1}$ (see Fig. 1). The directions $\mathbf{v}_u^n$ ($\mathbf{v}_s^n$) in Σ_n which are mapped onto the largest (shortest) semiaxis of the ellipsoid in Σ_{n+1} can be obtained by use of the singular value decomposition $A^n = U^nW^nV^{n\dagger}$ or equivalently by use of the polar decomposition $A^n = Q^nP^n$, $P^n = (A^{n\dagger}A^n)^{1/2}$. In the
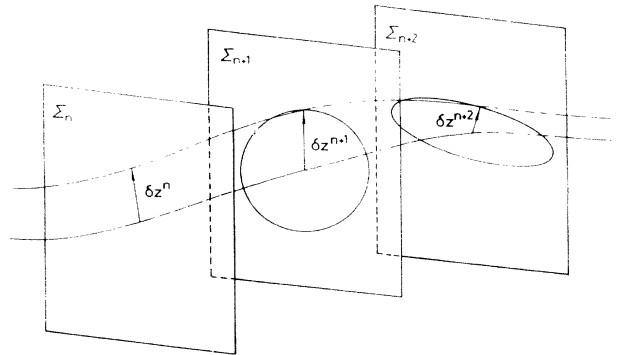

FIG. 1. At time step n the control perturbation δp^n is chosen such that the difference vector $\delta\mathbf{z}^n$ is mapped by A^n versus the stable direction $\mathbf{v}_s^{n+1}$ which will maximally shrink under the action of A^{n+1}.

first formulation $\mathbf{v}_u^n$ ($\mathbf{v}_s^n$) are the row vectors of V^n corresponding to the largest (smallest) singular value μ_u^n (μ_s^n), in the second $\mathbf{v}_u^n$ ($\mathbf{v}_s^n$) are just the eigendirections of the positive matrix P^n with eigenvalues μ_u^n (μ_s^n). To control the UPO the requirement of the local control method is now that δp^n has to be chosen such that the projection of $\delta \mathbf{z}^n$ onto the direction of maximal stretching $\mathbf{v}_u^n$ decreases every control step by a factor $(1 - \rho)$, i.e.,

$$\mathbf{v}_u^{n+1\dagger}\delta\mathbf{z}^{n+1} = (1 - \rho)\mathbf{v}_u^{n\dagger}\delta\mathbf{z}^n, \qquad 0 < \rho < 1. \tag{10}$$

Inserting Eq. (10) in (9) thus yields the control formula

$$\delta p^n = \frac{(1 - \rho)\mathbf{v}_u^{n\dagger}\delta\mathbf{z}^n - \mathbf{v}_u^{n+1\dagger}A^n\delta\mathbf{z}^n}{\mathbf{v}_u^{n+1\dagger}\mathbf{w}^n}. \tag{11}$$

For short control steps $\Delta t = \frac{T}{N} \to 0$, i.e., in the quasicontinuous limit, Eq. (11) can be simplified. Using the polar decomposition of the matrix $A^n = Q^n P^n = Q^n(\mu_u^n\mathbf{v}_u^n\mathbf{v}_u^{n\dagger} + \mu_s^n\mathbf{v}_s^n\mathbf{v}_s^{n\dagger})$ and the limit $Q^n \to 1$ and $\mathbf{v}_u^{n+1} \approx \mathbf{v}_u^n$ for $\Delta t \to 0$ we obtain the control formula

$$\delta p^n = (1 - \rho - \mu_u^n)\frac{\mathbf{v}_u^{n\dagger}\delta\mathbf{z}^n}{\mathbf{v}_u^{n\dagger}\mathbf{w}^n}. \tag{12}$$

With this formula it becomes evident why for short control steps Δt it is necessary to introduce the factor $(1 - \rho)$. In the quasicontinuous limit μ_u^n is of the order of 1. Furthermore, $\mathbf{w}^n = \frac{\partial \mathbf{P}^{(n,n+1)}}{\partial p} = \frac{\partial \phi_{\Sigma n}^{\Delta t}}{\partial p} = \frac{\partial \mathbf{v}(\mathbf{z},t_n)}{\partial p}\Delta t$ (where $\mathbf{v}$ is the nonautonomous vector field generating the flow ϕ) is proportional to Δt. Therefore, a small decay rate ρ cancels the singularity occurring in (12) and the necessary parameter perturbation δp_n will stay small as long as $\mathbf{z}^n$ is close to $\mathbf{z}_F^n$.

Analogous to the result in the preceding section the relation between the vectors $\mathbf{g}^n$,

$$\mathbf{g}^n\delta p \cong \mathbf{z}_F^n(p_0 + \delta p) - \mathbf{z}_F^n(p_0) \tag{13}$$

representing the shift of the UPO in Σ_n caused by the parameter perturbation, and the vectors $\mathbf{w}^n$ can be calculated as

$$\mathbf{w}^n = \mathbf{g}^{n+1} - A^n\mathbf{g}^n. \tag{14}$$

Note that in the derivation of the control formulas (11) or (12) it has never been used that the successive points $\mathbf{z}_F^n$ are intersections of an UPO with Σ_n. If one does not count n as n modulo N the local control method allows to follow every aperiodic orbit.

II. EXPERIMENTAL SETUP

A. The driven pendulum

In Fig. 2 the setup of the pendulum experiment is shown. The mechanical pendulum is designed such that its motion may be well approximated by the equation of motion:

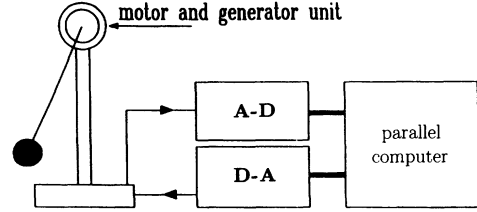$$I\frac{d^2\vartheta}{dt^2} + R\frac{d\vartheta}{dt} + M\sin\vartheta = A\sin\Omega t + B. \tag{15}$$

FIG. 2. Setup of the pendulum experiment. The electric motor is driven by a voltage $U(t) = U_A\sin(\Omega t) + U_B$ provided from the parallel computer. U_B serves as the control parameter. The tachogenerator detects the angular velocity $\dot{\vartheta}$. The $\dot{\vartheta}$ signal is processed in an electronic circuit in order to provide the ϑ and $\ddot{\vartheta}$ signals.

In this equation the variable ϑ denotes the angle of deflection and the constants I and R represent the coefficients of inertia and friction, respectively. The constant M is an abbreviation of the restoring moment mgl, with mass m and length l of the pendulum and gravitationally acceleration g. A is the amplitude of the harmonically driving torque, Ω its frequency, and B represents a constant torque. A and B are proportional to the voltages U_A and U_B, respectively, which are applied to the electric motor of the pendulum as $U(t) = U_A\sin\Omega t + U_B$ in order to generate the driving torque. U_B will be used as the accessible control parameter p_0. The maximal amplitude which can be applied to the electric motor is $U_A = 6$ V while the driving frequency Ω can be varied from 0.5 Hz to 1.6 Hz.

According to Eq. (15) the natural choice for the coordinates of the state space is $(\vartheta, \dot{\vartheta}, \psi)$ with the angular deflection ϑ, its velocity $\dot{\vartheta}$, and the phase $\psi = \Omega t$ of the driving. To measure the state space coordinates of the real pendulum and to control the motion of the pendulum a special electronic setup has been developed which is connected to a computer network equipped with digital-analog and analog-digital converters (Fig. 2).

The angular velocity $\dot{\vartheta}$ is directly measured by the voltage of a tachogenerator which is connected to the axis of the pendulum. In order to measure $\dot{\vartheta}$ in units of $2\pi\,\mathrm{rad/s}$ one has to multiply this voltage with a proper factor which can be obtained by measuring the generator voltage for a permanent rotation of the pendulum under constant driving torque. (The pendulum has to rotate in a horizontal plane to this end.) The average velocity is then determined as $\frac{2\pi}{T}$ with the period T of the rotation.

The variable ϑ is obtained by integrating the $\dot{\vartheta}$ signal. This integration is carried out by a voltage to frequency converter driving a digital 12-bit counter unit. The sign of $\dot{\vartheta}$ selects the up and downward direction of counting, respectively. The amplification in the circuit is chosen such that full deflection of the pendulum corresponds to an overflow of the counter, restricting the interval of integration to an interval representing $[-\pi, \pi]$. The integration as described above sums up errors due to asymmetries in the generator unit and hence it has to be corrected repeatedly. Furthermore, a starting point for the integration must be supplied in order to obtain an ab-

solute value of the angular position. Both requirements are satisfied by detecting the signal from the reflective object sensor in the base of the pendulum which is used to set the output of the integrator to zero, when the pendulum passes the bottom position.

The voltage U_A for the periodic driving torque as well as the voltage offset for the control signal U_B is produced by the parallel computer network driving a digital-analog converter. Hence the phase ψ has not to be measured separately as it is already on hand in the computer.

For the flow vector field analysis which is used to obtain the coefficients of the equation of motion from the experiment the acceleration $\ddot{\vartheta}$ has to be measured, too. $\ddot{\vartheta}$ can be obtained by differentiation of the velocity signal using a standard analog circuit based on operational amplifiers. To get the conversion factor from the voltage output of the amplifier to $\ddot{\vartheta}$ in units 2π rad/s^2, the circuit is calibrated by a sinusoidal signal, which can be obtained from the pendulum swinging at small amplitudes with frequency Ω_0, when $\ddot{\vartheta}$ corresponds to a value of $\ddot{\vartheta} = -\Omega_0^2 \vartheta$.

For further numerical analysis it is appropriate to rewrite Eq. (15) as

$$\vartheta'' + \gamma\vartheta' + \sin\vartheta = a\sin\omega\tau + b \; . \tag{16}$$

Herein $\tau = \Omega_0 t$ is a dimensionless time with $\Omega_0 = \sqrt{M/I}$ being the eigenfrequency of the unforced pendulum for small amplitudes. ϑ' and ϑ'' denote the derivatives with respect to τ. γ and a are the dimensionless coefficient of friction and the dimensionless driving amplitude respectively. The relations between the parameters in Eqs. (15) and (16) are thus given by $\gamma = \sqrt{R^2/IM}$, $a = A/M$, and $\omega = \Omega/\Omega_0$.

The control of the pendulum is carried out in the state space of the variables ϑ, ϑ', and $\psi = \omega\tau = \Omega t$. The attractor of the chaotic motion of the pendulum in these coordinates is shown in Fig. 3 for a Poincaré section corresponding to $\psi = 0$. The control parameter is set to $U_B = 0$, while $U_A = 6$ V and $\Omega = 0.83 \cdot 2\pi$ Hz are chosen such that the pendulum moves well in the chaotic regime.

B. The bronze ribbon

The second experiment is stimulated by the magnetoelastic buckled beam experiment of Moon [23]. In our case we have a horizontally cantilevered elastic bronze beam equipped with two small permanent magnets at its free end (see Fig. 4). The beam is located in an inhomogeneous magnetic field produced by two bigger permanent magnets. The resulting magnetic force $F \sim \partial B/\partial r$, where r is the position of the dipole at the tip of the ribbon, destabilizes the straight unbent position of the ribbon and creates two stable equilibrium positions of the bronze ribbon.

To drive the system two coils are placed around the free end of the beam. When the coils are supplied with an ac voltage $U(t)$ the beam starts to vibrate. For the experiment $U(t)$ is chosen as $U(t) = U_A \sin\omega t + p$. The amplitude $U_A = 0.7$ V is kept fixed and p is selected as control parameter for the feedback control. In our experiment p can vary between $(-1, 1)$ V and its value is obtained via a 12-bit resolution digital-analog converter from a 486 PC.

The dynamics of the beam is recorded using a wire strain gauge which measures the curvature near the base of the ribbon. It gives a voltage signal x which has a monoton relation to the deflection of the tip. The voltage is measured in the range of $(-0.5, 0.5)$ V and is transferred to the PC using a 12-bit resolution analog-digital converter. The output voltage is sampled at a frequency of $64/T$, where $T = 2\pi/\omega$ is the period of the forcing term $U(t)$. This implies that we can use maximally 64 Poincaré sections for the local control within our experimental setup.

In our experiments the period of the excitation is chosen to be $T = 1$ s. With this driving the ribbon vibrates chaotically when the control parameter is set to $p = 0$ V which will be our parameter p_0 where we want to control the ribbon. In Fig. 5 we present a bifurcation diagram
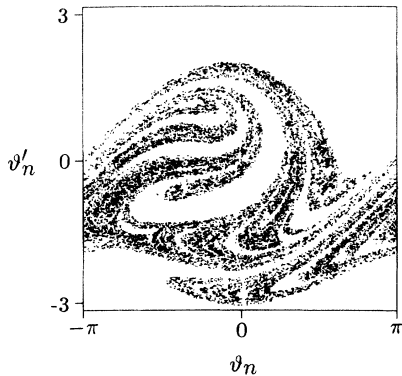
FIG. 3. The chaotic attractor of the driven pendulum in the Poincaré section $\psi = 0$. The driving period of the external torque is $T = 1.2$ s. The Hausdorff dimension for this attractor can be determined to $D_H \approx 2.8$.
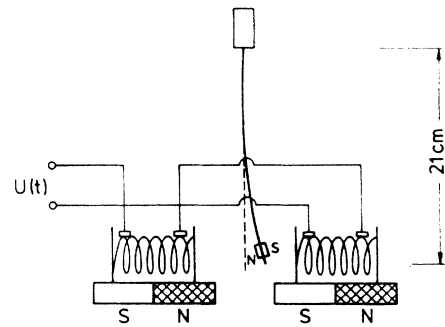
FIG. 4. Experimental setup of the chaotic bronze ribbon. A horizontally cantilevered bronze beam equipped with two small permanent magnets is located in an inhomogeneous magnet field. Two coils are placed around the free end of the beam and are supplied with an ac voltage $U(t) = U_A \sin\omega t + p$. The offset voltage p is the control parameter used in the experiment. Measurements are taken with a wire strain gauge at the end of the beam to obtain a voltage signal x related to the deflection of the beam.
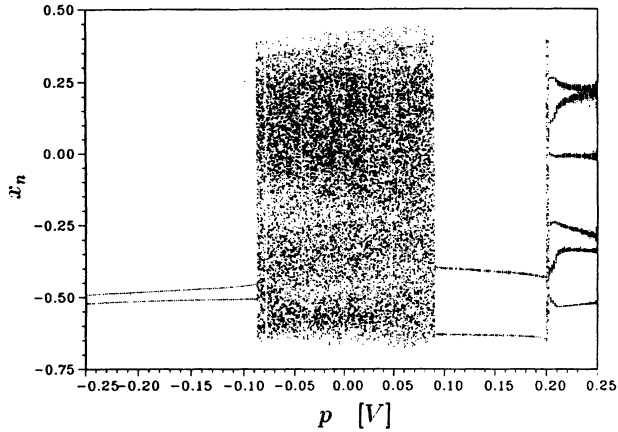
FIG. 5. Experimental bifurcation diagram of the bronze ribbon. Varying the offset voltage of the coils p as control parameter the stroboscopic measurements $x_n = x(nT)$ corresponding to $(z_n)_1$ in the Poincaré section Σ_0 are plotted versus p.

FIG. 7. Chaotic attractor for the bronze ribbon for $p = 0$ V. 100 000 points $z_n = (x_n, \dot{x}_n)$ are shown in the Poincaré section Σ_0.

of the experiment. For the control parameter p varying from -0.25 V to 0.25 V stroboscopic measurements of $x_n = x(nT)$ are plotted. Around $p = 0$ V a broad chaotic region can be detected. In Fig. 6 for $p = 0$ the first return map, x_{n+1} versus x_n, is plotted. As can be seen this map is fully two dimensional and cannot be reduced to a one-dimensional map.

To reconstruct the dynamics of the beam we proceed with a three-dimensional embedding having in mind that a one-mode approximation for a damped beam with a free end should describe the beam's equation of motion to first order. As state space coordinates $(x(t), \dot{x}(t), \theta(t))$ with $\theta(t) = t \bmod T$ was chosen. Because of the periodic driving the choice of θ as third coordinate is a rather natural one. It facilitates taking the Poincaré sections consider-
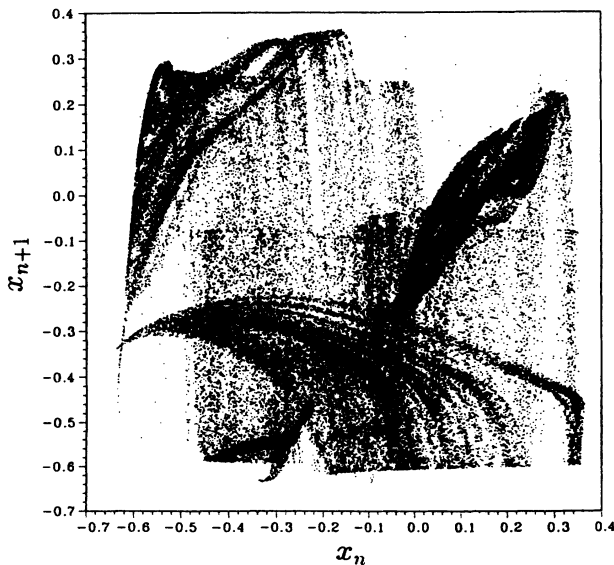

FIG. 6. First return map of the bronze ribbon for $p = 0$ V. $x_{n+1} = x[(n+1)T]$ versus $x_n = x(nT)$ is plotted.
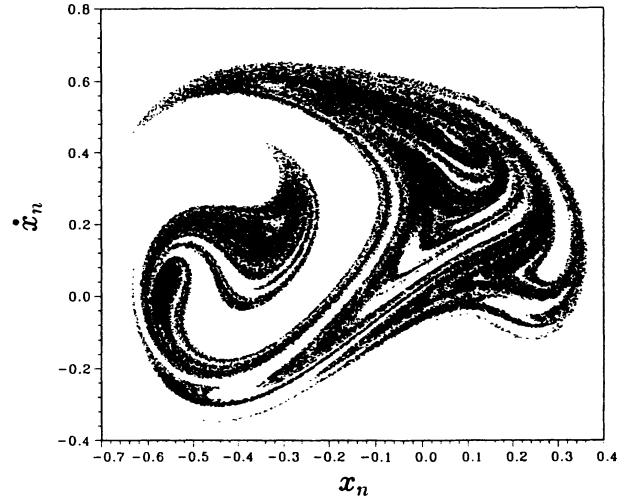
ably. One only has to set $\theta = \text{const}$. The velocity $\dot{x}(t_i)$ is estimated from the measurement signal by numerical differentiation. As time difference the sampling time Δt, in our case $1/64$ s, has been taken. The velocity $\dot{x}$ was scaled with a factor $1/10$ such that the state space coordinates x and $\dot{x}$ varied within the same range. Thus we use as units of time $[10^{-1}$ s]. For 64 Poincaré sections this results in a time difference $\Delta t = 0.16\,[10^{-1}$ s] between two successive Poincaré sections.

In Fig. 7 the chaotic attractor of the experiment for $p = 0$ V is shown in the Poincaré section $\theta = 0$. A clear deterministic structure is visible. Therefore, it should be possible to apply the OGY-control scheme.

III. DETERMINATION OF THE CONTROL VECTORS FROM MEASUREMENTS

In order to apply the OGY- and the local-control method to the two experiments described in the previous section, the control vectors have to be extracted from experimental data. To do this one has to determine the UPO's z_F^n, the linearizations A of the global, and A^n of the local Poincaré mappings for these UPO's as well as the vectors $\mathbf{g}$ or $\mathbf{w}$ and $\mathbf{w}^n$. In order to obtain optimal control vectors for the OGY control all necessary quantities are determined in every Poincaré section Σ_n. For further reference we introduce the notation

$$\mathbf{P}_n^G := \phi_{|\Sigma_n}^T ,\tag{17}$$

$$A_n^G := D_z \mathbf{P}_n^G(z_F^n) ,\tag{18}$$

$$\mathbf{w}_n^G := \frac{\partial \mathbf{P}_n^G}{\partial p}(z_F^n, p_0) .\tag{19}$$

When we consider the OGY control in our standard section Σ_0 we use the notation of Sec. 1.1, i.e., $A = A_0^G$, $\mathbf{w} = \mathbf{w}_0^G$, $\mathbf{g} = \mathbf{g}^0$.

Generally there are two possible approaches to extract

the control vectors. One may calculate them from a global mathematical model or utilize local fits around recurrent points in the embedding space. While for the pendulum both approaches are successful, for the bronze ribbon only local fits turn out to be feasible. In this section we first determine the global model for the pendulum and calculate the control vectors from this model. We then discuss the determination of the control vectors for the bronze ribbon using fits for recurrent points.

A. Flow field analysis for the pendulum

In order to achieve a global mathematical model of the pendulum, we have to determine the constants of the pendulum's equation (16). For this purpose we adapt the flow vector field analysis, introduced by Cremers and Hübler [18] to our needs.

The flow vector field analysis is based on N measurements

$$\{(\ddot{\vartheta}_i, \dot{\vartheta}_i, \vartheta_i, U_i)\}, \quad i = 1, \ldots, N , \qquad (20)$$

with $U_i = U(t_i)$ denoting the voltage applied to the electric motor to drive the pendulum. Assuming that the motion of the system can be described by a second order differential equation each of these measurements must fulfill an equation

$$\ddot{\vartheta}_i = F(\vartheta_i, \dot{\vartheta}_i, U_i), \quad i = 1, \ldots, N. \qquad (21)$$

To estimate F from the measurements we would like to use a polynomial expansion of F. As we expect the pendulum equation to describe the data a polynomial expansion of F could not be restricted to low order in ϑ^n because the Taylor expansion of $\sin \vartheta$ would enter the expansion. To avoid this we replace ϑ by $\sin \vartheta$ and use as ansatz for the equation of motion

$$\ddot{\vartheta}_i = P(\sin \vartheta_i, \dot{\vartheta}_i, U_i).$$

Further we expand P only by polynomials up to first order in each variable, thus we consider

$$\ddot{\vartheta} \cong c_1 \sin \vartheta + c_2 \dot{\vartheta} + c_3 U(t). \qquad (22)$$

The coefficients in (22) are determined by a least squares fit using about $N = 1000$ measurement data. In order to improve our model of the real pendulum, we have also tried polynomials of higher order than one. The results were almost vanishing coefficients of the nonlinear terms. Having thus obtained the coefficients c_1, c_2, c_3 one has to compare (22) and (16) in order to obtain the correct values of the constants in Eq. (16). Considering $\vartheta' = \dot{\vartheta}/\Omega_0$ and $\vartheta'' = \ddot{\vartheta}/\Omega_0^2$ this yields

$$\vartheta'' - \frac{c_2}{\Omega_0} \vartheta' - \frac{c_1}{\Omega_0^2} \sin \vartheta = \frac{c_3}{\Omega_0^2} U(\tau) \qquad (23)$$

and, finally, $\Omega_0^2 = -c_1$, $\gamma = -c_2/\Omega_0$, $a = \max\{c_3/\Omega_0^2 \cdot U(\tau)\}$, and $b = U_B c_3/\Omega_0^2$. For the flow field analysis $U(\tau) = U_A \sin \omega \tau = U_A \sin \Omega t$ has been used.

For the experimental parameters we use in our experiments we find the coefficients $\gamma = 0.052$, $\omega = 0.66$, and $a = 0.59$. Thus the differential equation

$$\vartheta'' + \gamma \vartheta' + \sin \vartheta = a \sin \omega \tau + b$$

together with the obtained coefficients and $U_B = b \Omega_0^2/c_3$ as control parameter is the global model we use to describe and to control the experimental pendulum.

B. Control vectors from the model

Having a differential equation as global model the calculation of the control vectors is straightforward. The UPO's are determined by a standard Newton algorithm. For the parameters of our model (16) we find ten different UPO's of period one.

Before we present the calculation of the linearization A^n of the local Poincaré mappings $\mathbf{P}^{(n,n+1)} = \phi_{|\Sigma_n}^{\Delta t}$, we want to mention its approximation for small Δt. Consider a nonautonomous system $\dot{\mathbf{z}} = \mathbf{v}(\mathbf{z}, t) = \mathbf{v}(\mathbf{z}, t + T), \mathbf{z} \in \mathbb{R}^2$, where the Poincaré sections of the equivalent autonomous system is taken at constant times t_n (or constant phases of the driving). It comes right from the definition that for (infinitesimally) small Δt

$$\varphi_{|\Sigma_n}^{\Delta t}(\mathbf{z}) \cong \mathbf{z} + \mathbf{v}(\mathbf{z}, t_n) \Delta t \qquad (24)$$

holds. For the quantities of interest in our control problem this leads immediately to

$$A^n \cong 1 + D_{\mathbf{z}_F^n} \mathbf{v}(\mathbf{z}_F^n, t_n) \Delta t \qquad (25)$$

and

$$\mathbf{w}^n \cong \frac{\partial \mathbf{v}}{\partial p}(\mathbf{z}_F^n, t_n) \Delta t. \qquad (26)$$

Specializing further to a nonautonomous system derived from a differential equation of second order, i.e., $\ddot{x} = f(x, \dot{x}, t)$, and choosing $(x, \dot{x}, t \bmod T)$ as state space coordinates, Eqs. (25) and (26) can be rewritten as

$$A^n \cong \begin{pmatrix} 1 & \Delta t \\ \frac{\partial f}{\partial x} \Delta t & 1 + \frac{\partial f}{\partial \dot{x}} \Delta t \end{pmatrix} \qquad (27)$$

and

$$\mathbf{w}^n \cong \begin{pmatrix} 0 \\ \frac{\partial f}{\partial p} \Delta t \end{pmatrix}. \qquad (28)$$

Taking into account the global model of the pendulum (16) we obtain approximations of the matrices A^n for the pendulum as

$$A^n \cong \begin{pmatrix} 1 & \Delta \tau \\ -\Delta \tau \cos \vartheta^n & 1 - \gamma \Delta \tau \end{pmatrix}. \qquad (29)$$

For the parameter dependence on the control parameter b Eq. (26) implies for small $\Delta \tau$

$$\mathbf{w}^n \cong \begin{pmatrix} 0 \\ \Delta \tau \end{pmatrix}. \qquad (30)$$

CONTROLLING CHAOS EXPERIMENTALLY IN SYSTEMS ...

The exact A^n can be obtained by integrating (16) together with its variational equations. We find that for $\Delta t = T/64, T = 1.2$ s there are only small deviations of these exact matrices from the approximation (29).

To calculate the dependence of the control parameter $\mathbf{w}^n$ we first determine $\mathbf{g}^n$ using (13) and $\delta p = \delta b = 0.0001$ followed by evaluation of Eq. (14). Again we find that the approximation (30) gives acceptable results for $\mathbf{w}^n$ for $\Delta t = T/64$. Having A^n, $\mathbf{w}^n$ the control formulas are calculated as described in Sec. I B.

For the OGY control the evaluation of the control vectors follow the same line. We use Newton's algorithm to determine the UPO's and integrate the variational differential equations to determine the linearization A or A_n^G taking as initial conditions $\mathbf{z}_F^n$ and ψ^n corresponding to the considered Poincaré section Σ_n. The control formulas are then evaluated as described in Sec. I A.

C. Control vectors from recurrent points—the bronze ribbon

For the bronze ribbon we did not succeed yet to extract a global model from the data. Therefore the control vectors have to be calculated solely from the dynamical behavior near recurrent points in the Poincaré section [24,25,2].

1. Unstable periodic orbits

As for the local control the intersection $\mathbf{z}_F^n$ of the UPO with each Poincaré section Σ_n, $n = 1, \ldots, N$, is needed m best recurrent points in every section Σ_n are recorded, i.e., we look for pairs of points $(\mathbf{z}^{n_i}, \mathbf{z}^{n_i+N})$, $\mathbf{z}^{n_i}, \mathbf{z}^{n_i+N} \in \Sigma_n$, $n_i \bmod N = n$, with

$$\|\mathbf{z}^{n_1} - \mathbf{z}^{n_1+N}\| \leq \|\mathbf{z}^{n_2} - \mathbf{z}^{n_2+N}\| \leq \cdots \leq$$

$$\leq \|\mathbf{z}^{n_m} - \mathbf{z}^{n_m+N}\| \leq \min_{\mathbf{z}^k \in \Sigma_n, k \neq n_i} \|\mathbf{z}^k - \mathbf{z}^{k+N}\|.$$

To find the correct grouping of the recurrent points into classes belonging to the same UPO the classification scheme described in [5] is adopted. In one selected Poincaré section, the *classification section* Σ_{n_c}, the best recurrent point $\mathbf{z}^{n_1} \in \Sigma_{n_c}$ is taken as master point of the first class. The second best recurrent point $\mathbf{z}^{n_2} \in \Sigma_{n_c}$ is classified to be in the same class if its distance to $\mathbf{z}^{n_1}$ is less than a maximum distance parameter ϵ, if not $\mathbf{z}^{n_2}$ forms the master point of the second class and so on. Having thus obtained a classification in Σ_{n_c} the best recurrent point of the other sections have to be classified according to the classes in Σ_{n_c}. For this purpose we record not only the recurrent points $\mathbf{z}^n, \mathbf{z}^{n+N} \in \Sigma_n$ but also $\mathbf{z}^{n'} \in \Sigma_{n_c}$, $n \leq n' \leq n + N$, i.e., the corresponding intersection point in the classification section. This intersection point is used to classify the best recurrent point in every Poincaré section Σ_n taking the existing classes in Σ_{n_c} thus assuring that, e.g., class one in every

section belongs to the intersection of the same UPO, and so on. The UPO $\{\mathbf{z}_F^n\}$ from a selected class of recurrent points is then estimated as weighted average of the recurrent points in each section using the reciprocal recurrent distances $1/\|\mathbf{z}^n - \mathbf{z}^{n+N}\|$ as weights.

In the experiment of the bronze ribbon three unstable period-one orbits could be detected. They are shown in Fig. 8. To obtain them 1000 best recurrent points in each section out of 100 000 periods have been used. For further reference they are called UPO 1, UPO 2, UPO 3.
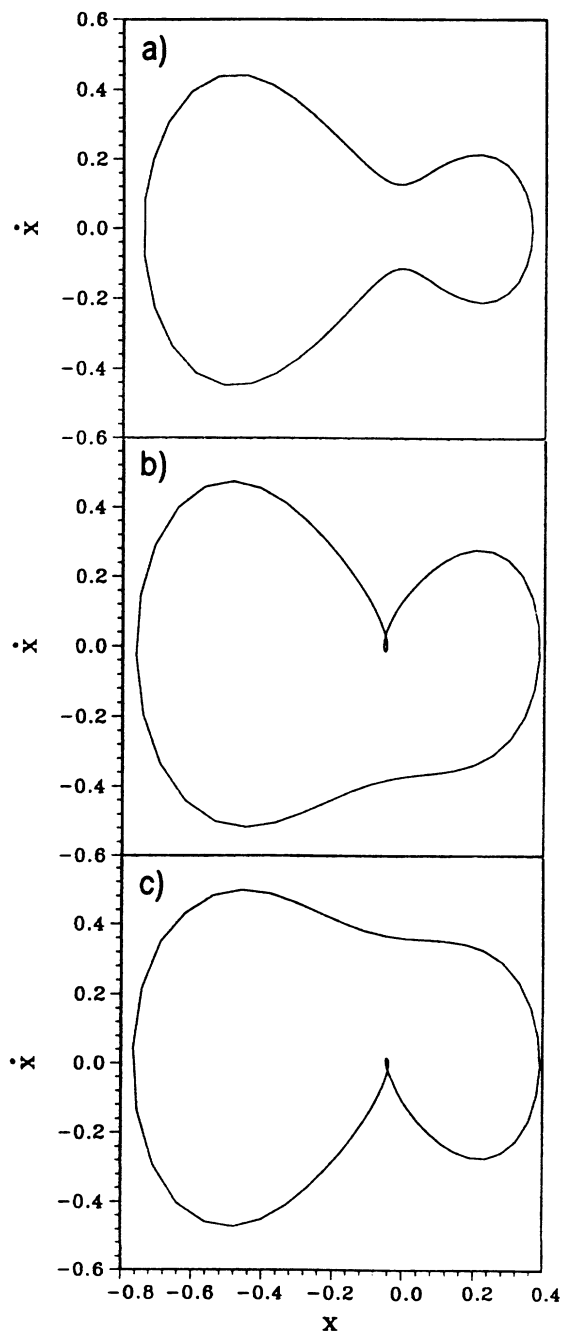

FIG. 8. The three unstable period-one orbits of the bronze ribbon which have been detected analyzing best recurrent points for $p = 0$ V. They are shown in the x-$\dot{x}$ plane and are named (a) UPO 1, (b) UPO 2, (c) UPO 3.

2. Linearizations A^n and A_n^G

To determine the linearization of the local Poincaré mappings $\mathbf{P}^{(n,n+1)}$ and the global mappings $\mathbf{P}_n^G$ for an UPO we do not use the already collected best recurrent points as was proposed in [5], we rather make a new run looking for the nearest neighbor points of the UPO $\{\mathbf{z}_F^n\}$, regardless whether they are best recurrent points or not. This effort turns out to be worthwhile since for systems with large unstable eigenvalue λ_u and even larger

quotient λ_u/λ_s of $\mathbf{P}_n^G$ the best recurrent points $\mathbf{z}^n$ are mostly placed along the stable direction $\mathbf{e}_s$ of $\mathbf{z}_F^n$ and its images $\mathbf{z}^{n+N}$ along the unstable direction $\mathbf{e}_u$ [see Fig. 9 (a)]. Thus considering only the best recurrent points for the fit of the linear mappings we would overweight these directions. Nearest neighbor points in contrast give also information about other directions [see Fig. 9 (b)] and thus give better approximations of the full linear mappings A_n^G and A^n.

To extract the mapping A^n and A_n^G from the dynamics of the nearest neighbors we record in each section beside the m nearest neighbor points $\mathbf{z}^{n_i} \in \Sigma_n$ itself also $\mathbf{z}^{n_i+1}$ and $\mathbf{z}^{n_i+N}$. Finally $A^n = D_{\mathbf{z}^n}\phi_{|\Sigma_n}^{\Delta t}$ and $A_n^G = D_{\mathbf{z}^n}\phi_{|\Sigma_n}^T$ are obtained from a least square fit using the relation

$$\mathbf{z}^{n_i+N} - \mathbf{z}_F^n = A_n^G \left(\mathbf{z}^{n_i} - \mathbf{z}_F^n\right) \qquad (31)$$

and

$$\mathbf{z}^{n_i+1} - \mathbf{z}_F^{n+1} = A^n \left(\mathbf{z}^{n_i} - \mathbf{z}_F^n\right). \qquad (32)$$

In Fig. 10 the linearization A^n of the local Poincaré mappings $\mathbf{P}^{(n,n+1)}$ are shown for the UPO 1. For each UPO continuous curves of the a_{ij}^n with respect to n are found. Furthermore, the calculated A^n agree nicely with the approximation (27) for the A^n which we expect to hold for small Δt. Note that a_{12}^n of our experimental A^n is almost constant, it only varies between 0.15 and 0.18. This is in agreement with $\Delta t = 0.16\,[10^{-1}\mathrm{s}]$ which we have as time difference between two successive Poincaré sections in our experiment. a_{11}^n and a_{22}^n are of the order of 1 as expected. The largest variation can be found in a_{21}^n which again coincides with the approximation (27). Thus the approximation (27) gives a good hint for the confidence one can have in the A^n obtained from the experimental data of the ribbon.

For the pendulum we also extracted the A^n from fits near recurrent points. Comparison between them and the A^n obtained from the global model also showed that it is no problem to extract the linearization of the local mappings with sufficient accuracy using only linear fits from measurement data.

The estimation of the linearization A_n^G of the global Poincaré mappings $\mathbf{P}_n^G$ proves to be much more difficult. First of all, the degree of nonlinearity of $\mathbf{P}_n^G$ is

FIG. 9. (a) Out of 100 000 periods 50 best recurrent points (+), $\mathbf{z}^n \in \Sigma_0$, belonging to the class of UPO 1 and their images ($\times$), $\mathbf{z}^{n+N} \in \Sigma_0$, under the Poincaré map $\mathbf{P}_0^G$ are shown. The two arrows are located at $\mathbf{z}_{F_1}^0$ and give the stable (filled vector) and unstable (open vector) eigendirections of the linearization $A_0^G = D_{\mathbf{z}_{F_1}^0}\mathbf{P}_0^G$ with eigenvalues $\lambda_u \approx 9$ and $\lambda_s \approx 0.1$ obtained using the product (33) of the local matrices A^n. As can be seen the best recurrent points are mostly placed along the stable direction while their images are mapped along the unstable direction due to the large ratio $\lambda_u/\lambda_s \approx 90$. (b) The 50 nearest neighbor points (+) $\mathbf{z}^n$ of $\mathbf{z}_{F_1}^0$ (•) are shown. They give information of the full linear mapping around $\mathbf{z}_{F_1}^0$.
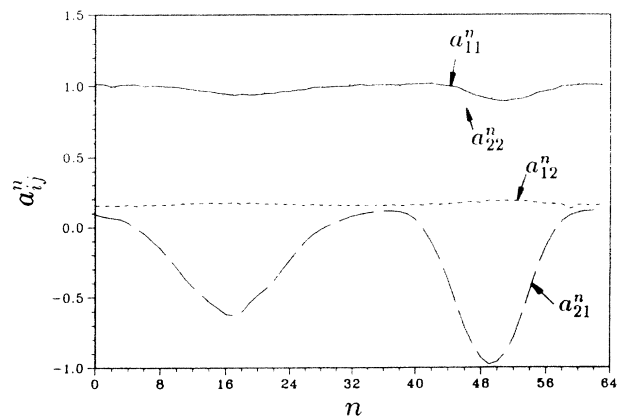

FIG. 10. Linearization $A^n = (a_{ij}^n)$ of the local Poincaré mappings $\mathbf{P}^{(n,n+1)}$ for the UPO 1 of the bronze ribbon.

certainly higher than of the (time) local Poincaré mappings $\mathbf{P}^{(n,n+1)}$. Therefore, in order to extract A_n^G one has to use smaller neighborhoods for the fit of A_n^G than for the A^n. Thus if the nearest neighbors are obtained from some fixed measurement, in our case 100 000 periods, one can only use less nearest neighbors for the fit of A_n^G

than one can use for the fits of the local mappings A^n. Alternatively, one has to make longer measurements.

Since there is no *a priori* knowledge on the form of the A_n^G, we use our knowledge about the eigenvalues λ_u^n, λ_s^n, of the A_n^G. As the eigenvalues of an UPO are invariant under a change of coordinates they have to be the same
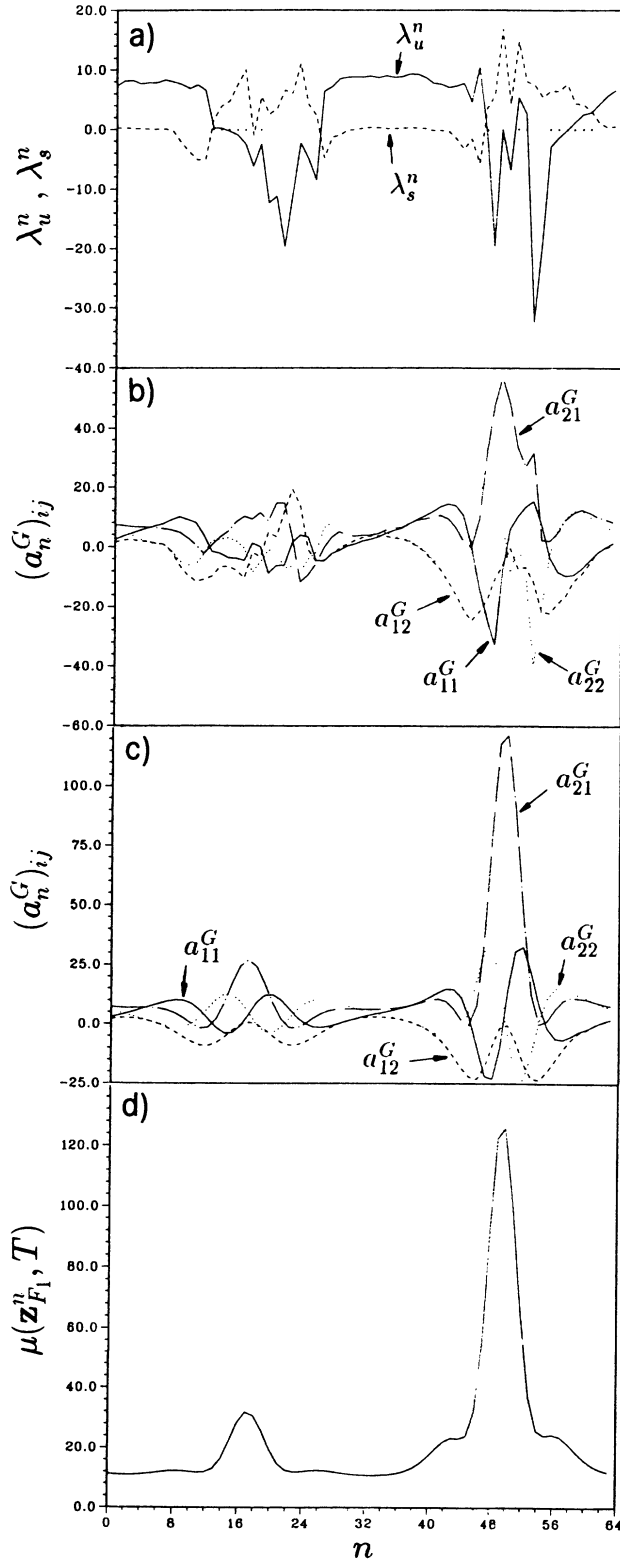
FIG. 11. Determination of the linearizations A_n^G of the global Poincaré mappings $\mathbf{P}_n^G = \phi_{|\Sigma_n}^T$ of UPO 1. (a) The eigenvalues λ_u^n (solid line), λ_s^n (dashed line) from A_n^G obtained from a direct fit using Eq. (31). The small dots indicate the n where the fit yields complex eigenvalues λ^n. Here the real (solid line) and the imaginary part (dashed line) of λ^n are plotted. (b) A_n^G from Eq. (31) versus n, (c) A_n^G calculated as a product of the local matrices A^n using Eq. (33), (d) the maximal singular values $\mu_n^u = \mu(\mathbf{z}_{F_1}^n, T)$ of the A_n^G shown in (c). As can be seen the problems of the fits in (a) and (b) are related to the large stretching rates μ_n^u in the corresponding Poincaré sections.

for every Poincaré section Σ_n. Furthermore, $|\lambda_u^n| > 1$ and $|\lambda_s^n| < 1$ should hold for an UPO lying in an attractor as well as $\lambda_u \cdot \lambda_s = \det D\phi_\Sigma^T > 0$ is valid for an UPO of a dynamic system generated by a vector field.

In Fig. 11 (a) the eigenvalues of A_n^G of UPO 1 are plotted versus n. As can be seen there are Poincaré sections where the eigenvalues fluctuate wildly. In these regions they even can become complex. However, there are also regions where λ_u^n and λ_s^n are independent of n as it should be. The level of these plateaus give us a first hint about the possible values of λ_u and λ_s. For UPO 1 we obtain $\lambda_u \cong 9$ and $\lambda_s \cong 0.1$. For the calculation of the A_n^G which are the basis of Fig. 11 $m = 60$ nearest neighbors have been used. We also varied the number of nearest neighbors between $m = 20$ and $m = 500$ and plotted λ_u^n and λ_s^n versus n. Increasing the numbers of nearest neighbors (and thus the size of the neighborhood) soon deteriorated the results for λ_u^n and λ_s^n. But already our best result in Fig. 11 (a) demonstrates how difficult the determination of A_n^G can be in the presence of some measurement noise when λ_u is of the order of 10 and $\lambda_u/\lambda_s \cong 100$.

Thus having difficulties to estimate A_n^G directly using only the dynamics (31) in one section we tried to get another estimate of A_n^G using the local mappings A^n obtained from (32) and the relation

$$A_n^G = A^{n+N-1} \cdots A^{n+1} A^n. \tag{33}$$

In Fig. 11 (b) and 11 (c) $(a_n^G)_{ij}$ are shown for the fitted A_n^G using Eq. (31) and the A_n^G calculated as a product of the A^n using Eq. (33). Although they differ considerably in their numerical value they show the same overall behavior. But even if the $(a_n^G)_{ij}$ in Fig. 11 (c) obtained by multiplication of the local A^n fluctuate wildly there eigenvalues λ_u^n and λ_s^n are constant as a function of n as it must be by construction. We obtain $\lambda_u^n = 8.5$ and $\lambda_s^n = 0.08$. These eigenvalues are in good agreement with the eigenvalues obtained from the plateaus in Fig. 11 (a) confirming the estimate of λ_u and λ_s. In Fig. 11 (d) finally we plotted the largest singular value $\mu(\mathbf{z}_F^n, T) = \exp(\lambda_{eff}(\mathbf{z}_F^n, T)T)$ of A_n^G given by (33). As can be seen these singular values and thus the effective Lyapunov exponents become very large exactly in the regions where the eigenvalues λ_u^n and λ_s^n in Fig. 11 (a) fluctuate wildly which indicates that the A_n^G obtained from the direct fit (31) are not reliable. If one looks at the angle between the eigendirections $\mathbf{e}_u^n$ and $\mathbf{e}_s^n$ of A_n^G obtained from (33) it can be seen that in regions of large singular values the angle between the eigendirections diminishes. Because of the large Lyapunov exponents for these n even small measurement errors will lead to a bad estimate of A_n^G if only (31) is used. Thus the A_n^G obtained from (33) give a good explanation why the fit (31) does not give good results for some Poincaré sections. Furthermore, the eigenvalues of A_n^G from (33) fulfill all theoretical requirements about the eigenvalues of an UPO and coincide with the plateaus where the fit (31) seems to work. For our experiment we therefore always used A_n^G obtained from the product of the A^n to estimate the eigenvalues and eigendirections for the OGY control formula.

The results for the A_n^G of the other UPO's show the same finding as the just reported one for UPO 1. For
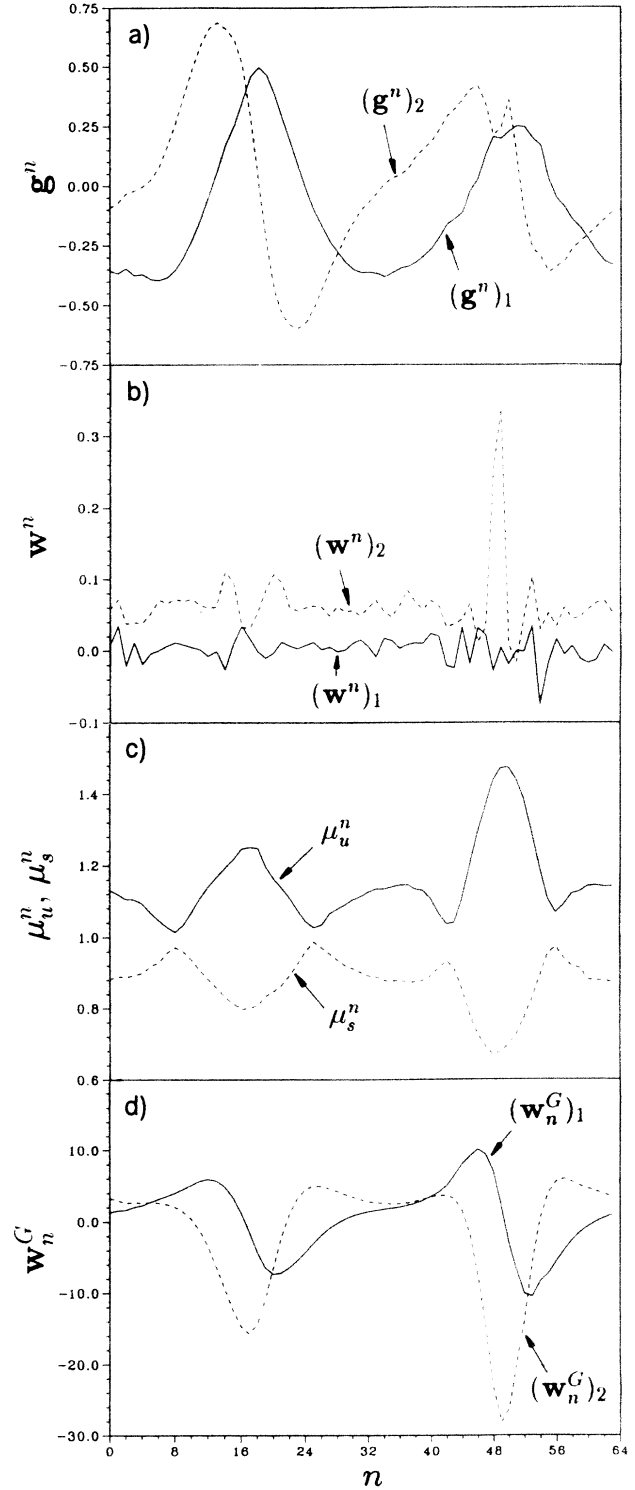

FIG. 12. For the bronze ribbon the dependence on the control parameter p is examined. Using a parameter change of $\delta p = -0.025, 0.025, -0.05, 0.05$ V the shift of the UPO $\mathbf{z}_F^n(p_0 + \delta p) - \mathbf{z}_F^n(p_0)$ are analyzed. For UPO 1 we show (a) the components of $\mathbf{g}^n = \frac{\partial \mathbf{z}_{F_1}^n}{\partial p}$, (b) the components of $\mathbf{w}^n = \frac{\partial \mathbf{P}^{(n,n+1)}}{\partial p}(\mathbf{z}_{F_1}^n, p_0)$, (c) the singular values of $A^n = D_{\mathbf{z}_{F_1}^n} \mathbf{P}^{(n,n+1)}$, and (d) $\mathbf{w}_n^G = \frac{\partial \mathbf{P}_n^G}{\partial p}(\mathbf{z}_{F_1}^n, p_0)$.

UPO 2 we estimate $\lambda_u = -13$, $\lambda_s = -0.05$ and for UPO 3 $\lambda_u = -11$ and $\lambda_s = -0.07$ looking both for the plateau of λ_u^n and λ_s^n and the λ_u and λ_s obtained from the product of A^n.

3. Dependence on the control parameter

To determine the sensitivity of the experiment to a change of the control parameter p the dependence $\mathbf{g}^n$ of the location of the fixed points $\mathbf{z}_F^n(p)$ in Σ_n have to be measured. For this purpose we run the experiment four times with a parameter change $\delta p = -0.025, 0.025, -0.05, 0.05$ [V] giving rise to four $\mathbf{g}^n$ using Eq. (13). As final $\mathbf{g}^n$ the average over these $\mathbf{g}^n$ is taken. The result is shown in Fig. 12 (a). Except around the Poincaré section $n = 48$ there is a smooth dependence of $\mathbf{g}^n$ with respect to n. In Fig. 12 (b) the resulting $\mathbf{w}^n$ calculated from (14) using $\mathbf{g}^n$ and A^n are presented. Although the underlying A^n (Fig. 10) and $\mathbf{g}^n$ seem to be determined with sufficient accuracy the values of $\mathbf{w}^n$ are much more noisy. The reason for this is that for small Δt the singular values of A^n [see Fig. 12 (c)] are of the order of 1, thus $\mathbf{g}^{n+1}$ and $A^n \mathbf{g}^n$ will not differ much. For the determination of $\mathbf{w}^n$ therefore a higher accuracy in more digits is necessary. Recalling the meaning of $\mathbf{g}^n$ and $\mathbf{w}^n$ as $\mathbf{g}^n$ being mainly the shift of the UPO when a permanent parameter change is applied and $\mathbf{w}^n$ being the dependence of the system when a perturbation is applied only for the time Δt it becomes evident that it must be much harder to determine $\mathbf{w}^n$ than $\mathbf{g}^n$.

Finally in Fig. 12 (d) the dependence $\mathbf{w}_n^G$ of the global Poincaré mappings $\mathbf{P}_n^G$, calculated from $\mathbf{w}_n^G = \mathbf{g}^n - A_n^G \mathbf{g}^n$, is shown. To obtain $\mathbf{w}_n^G$ the A_n^G in Fig. 11 (c) calculated from Eq. (33) have been used. As the eigenvalues of A_n^G are comparatively large there is no loss of accuracy taking the difference of $\mathbf{g}^n$ and $A_n^G \mathbf{g}^n$. As $\mathbf{w}_n^G$

characterizes the sensitivity of the system when a perturbation is applied over a whole period T they are much easier to determine than the $\mathbf{w}^n$ as long the determination of A_n^G is reliable. As $\mathbf{g}^n$ comes from first measurement these values are certainly more reliable than the $\mathbf{w}_n^G$. But for the calculation of the control vectors in (5) or (6) the A_n^G have to be used anyway. Therefore, the control vectors obtained from (5) or (6) turn out to be the same.

IV. EXPERIMENTAL RESULTS

A. Controlling the pendulum

In Fig. 13 we show the fixed points corresponding to ten period one UPO's in the section $\psi = 0$. To demonstrate that these orbits are highly unstable we superimpose a portrait of the largest effective Lyapunov exponent $\lambda_{eff}(\vartheta, \vartheta', T)$ [definition Eq. (1)] for a time interval corresponding to one driving period T in the same section. Dark zones in this portrait correspond to high values of $\lambda_{eff}(\vartheta, \vartheta', T)$ and indicate areas where predictions and also the control of the motion are highly affected by noise as pointed out in the introduction of this paper. All period one UPO's of the pendulum are well located in these dark regions. This is strongly related to the fact that the eigenvalues of the linearization of the Poincaré mappings for all of these orbits are comparatively large [26]: they vary from $|\lambda_u| = 12.2$ to $|\lambda_u| \approx 7800$. (The later one belongs to an orbit which tracks a swing with small amplitude around the point of overturn.)

We first test the original OGY-control ansatz in the experiment for different UPO's in various Poincaré sections. The control vectors for these experiments are calculated from the global model as discussed in Sec. III B. The control is activated only when the absolute control signal $|U_B|$ is smaller than a certain threshold $U_{B_{max}} = 0.2 U_A$. During the experiment we often observe that the motion of the system is close to the desired orbit triggering a perturbation of the control parameter. These control attempts nevertheless do not result in stabilization of an UPO in our experiments.

To test the local control method we select $N = 64$ control steps per driving period T of the periodic torque.
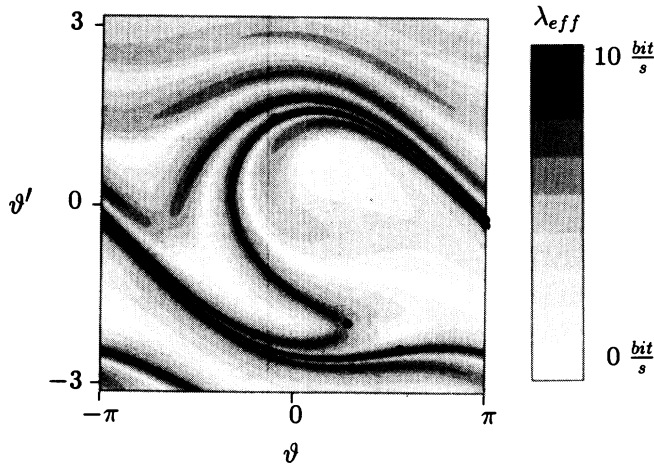

FIG. 13. Gray scale plot of the effective Lyapunov exponent $\lambda_{eff}(\vartheta, \vartheta', T)$ of the pendulum for the time T corresponding to one period of the driving in the Poincaré section $\psi = 0$. Dark zones indicate large exponents while bright zones correspond to low values of $\lambda_{eff}(\vartheta, \vartheta', T)$. The dots (•) indicate ten period one UPO's in the section $\psi = 0$. Without exception they are located in regions with large effective Lyapunov exponents.
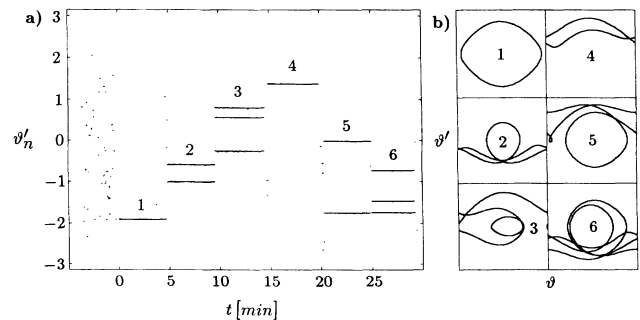

FIG. 14. Local control of UPO's of the pendulum. (a) The control is switched on at time $t = 0$, every five minutes the UPO to be controlled is changed. The stroboscopic angular velocity ϑ_n' is shown. (b) The corresponding unstable periodic orbits in the ϑ-ϑ' plane.
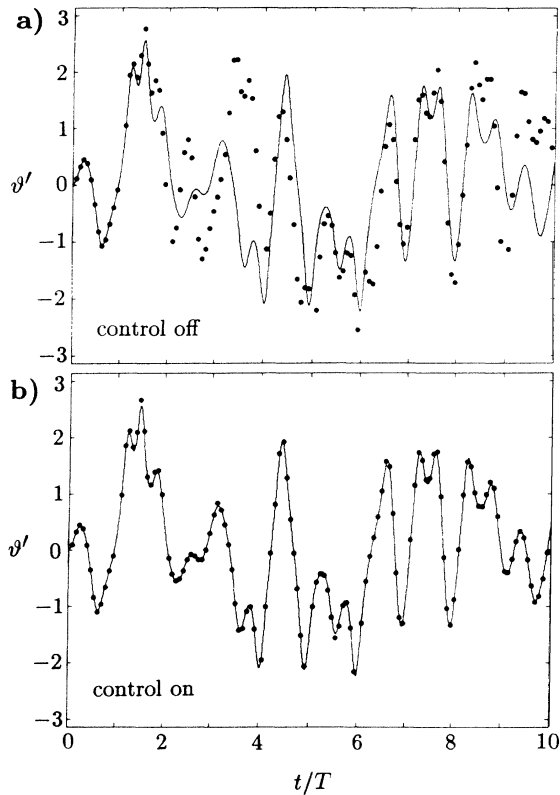
FIG. 15. Local control of a chaotic trajectory of the pendulum. Comparison of the velocity signal of the predicted target trajectory (solid line) and the actual motion of the experimental pendulum (dots). (a) Without control prediction and actual motion diverge. (b) With control the motion of the pendulum is kept close to the goal trajectory.

For the stabilization of the UPO's, we use the control vectors calculated from the global model as well as determined by local fits near recurrent points. The decay rate is set to $\rho = 0.15$. Again, we apply a control only when $|U_B| < U_{B,max} = 0.2U_A$.

This way we are able to stabilize every detected UPO regardless of the period of the orbit using local control. In Fig. 14, we present some of these different modes of motion up to a length of period three. In the figure we plot on the left side the angular velocity ϑ' at constant phase $\psi = 0$. In this plot chaotic motion of the system is marked by a broad distribution of the angular velocities as a function of time, while periodic motion is marked by lines of almost constant velocities. The number of lines displayed in each of the time intervals indicates the period of the periodic orbit.

We first observe chaotic motion of the pendulum when no control is applied. At time $t = 0$ local control is activated for the first orbit displayed on the right side of Fig. 14. After a short chaotic transient the periodic orbit is stabilized. In the following every five minutes the UPO to be controlled is changed to one of the orbits shown in Fig. 14. The time to achieve control after a change of the control vectors or when the system is disturbed externally is typically in the range of a few driving periods. We observe a kickout of the orbits only, when the

system is disturbed externally by a major perturbation, e.g., touching the rotor, etc.

To demonstrate control of a chaotic trajectory, the control vectors have to be calculated from the global model. Toward this end any solution of the equation of motion may be chosen as a *goal trajectory*. As an example, we calculate a prediction of the pendulum's motion based on an initial state measured from the system. In Fig. 15 (a) we present a comparison of the predicted velocity signal of the pendulum for the time interval 10 s with the observed motion of the pendulum when no control is applied. Due to the sensitive dependence on the initial state, prediction and actual motion of the pendulum diverge severely after about 2 s. In Fig. 15 (b) we show the velocity signal of a controlled motion for the same trajectory segment as in Fig. 15 (a). The motion of the pendulum stays close to the target curve as long as the control is activated.

B. Controlling the bronze ribbon

For the bronze ribbon we first tried to stabilize the three UPO's (Fig. 8) determined from the experiment using the OGY-control vectors suited to stabilize the system applying one control step per period. Although we avoided for this type of control the Poincaré sections with extremely high effective Lyapunov exponents like, e.g.,
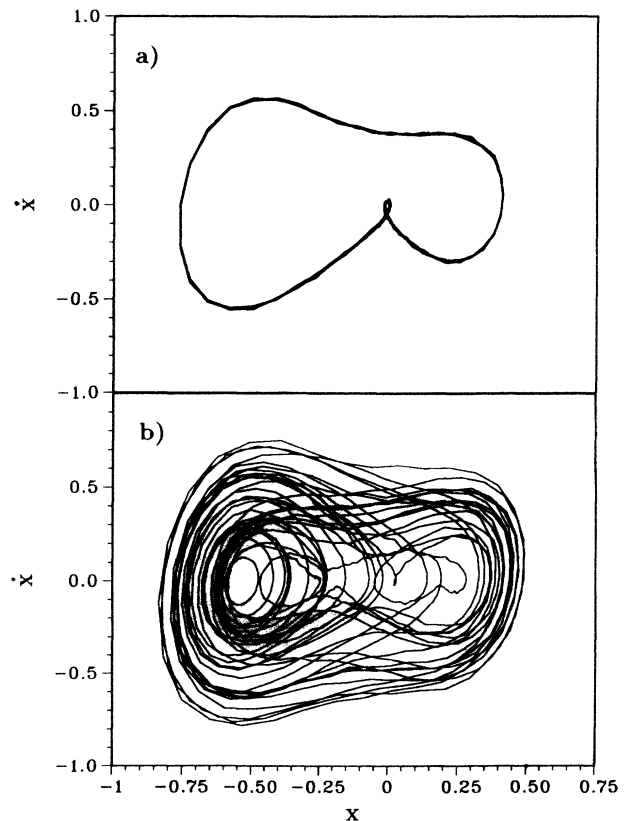

FIG. 16. Local control of the bronze ribbon: (a) 20 periods of the controlled ribbon in the x-$\dot{x}$ plane having UPO 3 chosen as desired orbit. (b) 20 periods of the uncontrolled motion of the bronze ribbon in the x-$\dot{x}$ plane.
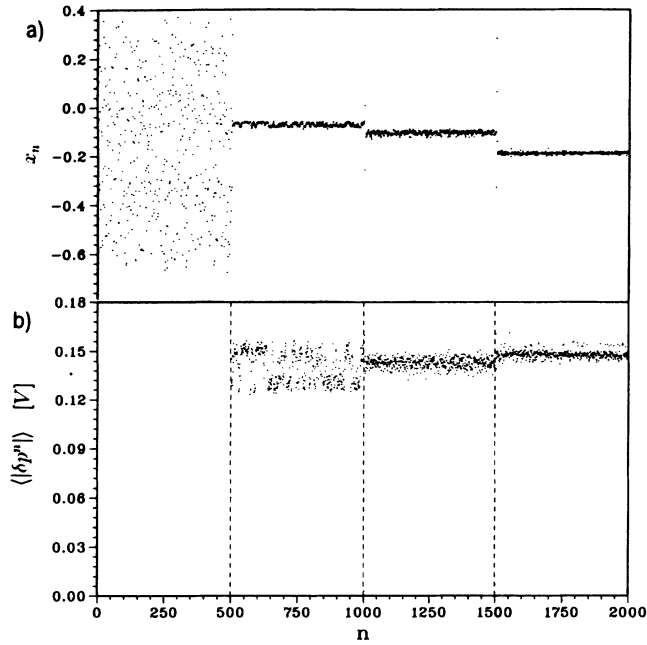
FIG. 17. Local control of the bronze ribbon: (a) First component $(z_n)_1 = x_n = x(nT)$ in the Poincaré section Σ_0 versus n. From 0 – 500 no control is applied. Using the local control formula (11), a maximal distance $\delta z_{max} = 0.3$ and the maximal parameter perturbation $\delta p_{max} = 0.18$ V the three UPO's are successively controlled. From $n = 501-1000$ UPO 1, from $n = 1001 - 1500$ UPO 2, and finally from $n = 1501 - 2000$ UPO 3. (b) The absolute value of the needed parameter perturbation averaged over one period of the driving plotted versus n.

section Σ_{50} of UPO 1 [Fig. 11 (d)] we never succeeded to reach control.

Next, we tried to control the ribbon by local control with the control vectors extracted from the analysis in Sec. III C. But this first attempt also failed. As was already discussed in Sec. III C 3 the $\mathbf{w}^n$ are noisy. Because they are small for small Δt and appear in the denominator of the control formulas (11) or (12) the resulting control vectors $\mathbf{K}^n$ of the local control, $\delta p^n = \mathbf{K}^n \delta \mathbf{z}^n$, are even more noisy. As a first remedy, one could remove the obvious glitches observed, e.g., in Σ_{48} of UPO 1 [Fig. 12 (b)] and smooth the $\mathbf{w}^n$. But this cannot prevent that the local-control vectors $\mathbf{K}^n$ can become very large in some sections Σ_n. In these sections the requirement $|\delta p^n| \leq \delta p_{max}$ is almost never fulfilled even when $\|\delta \mathbf{z}^n\|$ is small. Here the control will never be applied. Because of the high instability of the system these times of suspended control suffice to lead to a failure of control.

In order to keep the system for these critical time steps n under control we formulate the following control rule

$$
\delta p^n = \begin{cases} \mathbf{K}^n \delta \mathbf{z}^n & \text{if } \|\mathbf{K}^n \delta \mathbf{z}^n\| \leq \delta p_{max} \\ \text{sign}(\mathbf{K}^n \delta \mathbf{z}^n)\delta p_{max} & \text{if } \|\mathbf{K}^n \delta \mathbf{z}^n\| > \delta p_{max} \\ & \text{and } \|\delta \mathbf{z}^n\| \leq \delta z_{max} \\ 0 & \text{otherwise.} \end{cases} \quad (34)
$$

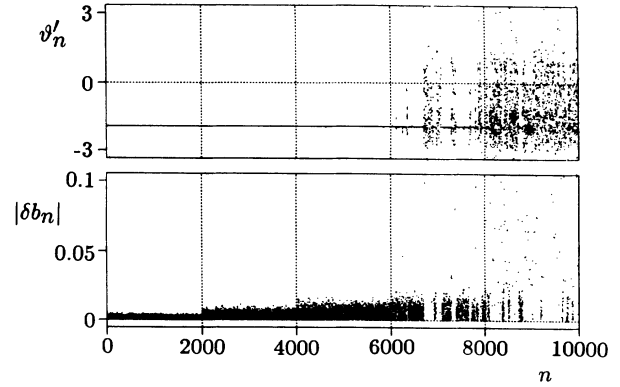Thus we continue the control if we are closer than a max-

imal distance δz_{max} even when the δp^n calculated from (11) or (12) exceed δp_{max}. In these cases we control but restrict the control force to $|\delta p^n| = \delta p_{max}$.

Using the control rule (34) we are able to control UPO 1, 2, and 3. In Fig. 16 (a) we show in the x-$\dot{x}$ plane the controlled trajectory of the bronze ribbon for 20 periods having chosen UPO 3 as UPO to be stabilized. In Fig. 16 (b) in contrast the trajectory of the uncontrolled ribbon for 20 periods of the driving is shown. If one suspends the control the ribbon almost immediately turns into the uncontrolled chaotic motion of Fig. 16 (b).

In Fig. 17 we use the local control with Eq. (11) to successively stabilize UPO 1, UPO 2, and UPO 3. As maximal distance $\delta z_{max} = 0.3$ and as maximal parameter perturbation $\delta p_{max} = 0.18$ V is chosen. As can be seen it only needs some periods to gain control if one switches from one UPO to the other. We have also tried the control formula (12) which should be a good approximation for large number of control stations N.

FIG. 18. Numerical control of an UPO of the pendulum with the original OGY control. In the upper part we show the ϑ' signal in the Poincaré section Σ_0, in the lower the absolute value of the control signal δb_n. Starting with a noise level $\epsilon = 0.001$ we increase the noise every 2000 driving periods by an amount of $\epsilon = 0.001$.
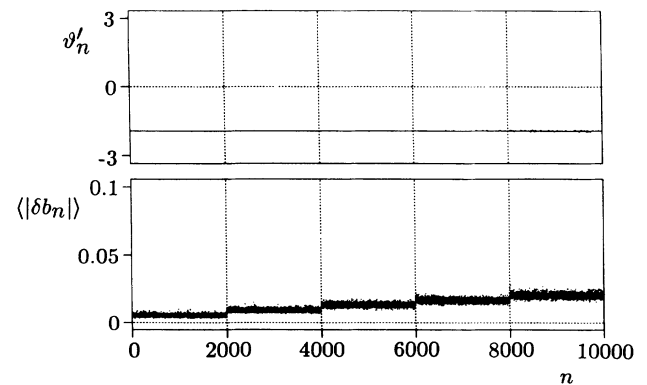

FIG. 19. Numerical control of an UPO of the pendulum with local control using $N = 100$ control steps per period. In the lower part we show the total of the control signal averaged over one driving period. Starting with $\epsilon = 0.01$ every 2000 driving periods the noise level is increased by $\epsilon = 0.01$.

For $N = 64$ the local control was also able to stabilize the different UPO's using Eq. (12). Referring to the approximation (28) for the $\mathbf{w}^n$ we even tried as ansatz for the $\mathbf{w}^n$, $\mathbf{w}^n = (0, k\,\Delta t)^\dagger$, with an appropriately chosen constant k. Substituting this crude approximation for the $\mathbf{w}^n$ into the control formula (11) or (12) we could stabilize the UPO's needing this time larger parameter perturbations. This shows that the local control is rather robust against a failure in the determination of the control vectors as long as one does not suspend the control and uses the control rule (34). For all control formulas nevertheless the stabilized motion can differ more or less from the desired unstable orbit. As in the tracking approach of Schwartz and Triandaf in [27] one could vary the control vectors and the goal UPO in order to diminish the necessary parameter perturbation and thus improve the control or in order to cope with slowly varying system parameters.

C. Numerical experiment—influence of noise

In the following, we investigate the robustness of the control methods with respect to noise. For this purpose we stabilize an UPO in a numerical experiment on the basis of the pendulum equation. Noise is introduced by adding small noise terms $\epsilon \cdot \delta$, $\epsilon \cdot \delta'$ to ϑ and ϑ', δ and δ' being identically distributed in $[-1, 1]$. Thus mimicking a noisy measurement of the $\delta \mathbf{z}^n$, we calculate the control amplitude using (5) and (12), respectively. The values of the control vectors in (5) and (12) itself are still taken from the equation of motion. Doing this we concentrate on the effect of errors in the determination of the state on the feedback control.

In Fig. 18 we present the effect of noise on the original OGY control. On top the ϑ' signal in the Poincaré section $\psi = 0$ is shown; on bottom the control parameter δb_n can be seen. Starting with a noise level $\epsilon = 0.001$ [note that the range of ϑ and ϑ' is about $(-\pi, \pi)$] we repeatedly increase the noise after 2000 driving periods by 0.001. As a result up to a level $\epsilon = 0.003$ the noise results mainly
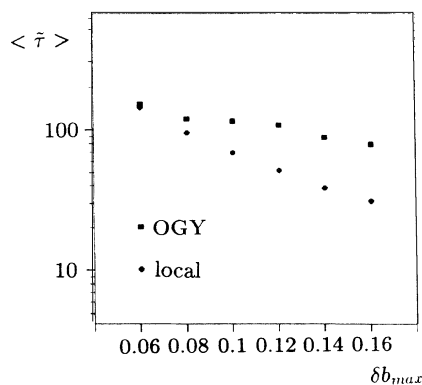

FIG. 20. The average time to achieve control $\langle \tilde{\tau} \rangle$ from a numerical experiment for a period one UPO of the pendulum as a function of the maximal allowed control perturbation δb_{max}. Squares mark the results for the original OGY control, circles for the local control using 100 control steps per period.

in an increase of the control parameter level, while the control remains stable. Beginning with $\epsilon = 0.004$ the control is no longer stable while for larger noise levels it fails completely.

The same numerical experiment is shown in Fig. 19 for the local control. Here in the bottom plot we show the absolute value of the control parameter $\langle |\delta b^n| \rangle$ averaged over one period of the driving. The first noise level is $\epsilon = 0.01$ which is by a factor ten larger than the noise in the experiment described above. Again, after each 2000 driving periods the noise is increased, this time by 0.01. Each raise of the noise increases $\langle |\delta b^n| \rangle$ but the control remains stable up to $\epsilon = 0.05$. Further increase of ϵ reveals occasional failures of the control for $\epsilon = 0.08$. Larger noise destroys the performance of the local control.

D. Transient times for the control in numerical experiment

An important characteristic of a chaos control method is the typical length $\tilde{\tau}$ of chaotic transients after the control has been activated before stabilization of the UPO occurs. For randomly chosen initial conditions this transient time $\tilde{\tau}$ has an exponential probability distribution [2] $p(\tilde{\tau}) \sim \exp[-(\tilde{\tau}/\langle \tilde{\tau} \rangle)]$ for large $\tilde{\tau}$. The characteristic length $\langle \tilde{\tau} \rangle$ is a function of the maximal allowed control parameter which for the pendulum is $\delta p_{max} = \delta b_{max}$. With increasing δb_{max} the average time to achieve control $\langle \tilde{\tau} \rangle$ decreases. We investigate the dependence of $\langle \tilde{\tau} \rangle$ on δb_{max} in a numerical simulation of the global model of the pendulum.

In Fig. 20 we plot $\langle \tilde{\tau} \rangle$ versus δb_{max} for the OGY method (squares) and for the local-control method (dots). Note that while for small δb_{max} $\langle \tilde{\tau} \rangle$ is nearly the same for the two control methods, for larger δb_{max} the values of $\langle \tilde{\tau} \rangle$ decreases faster for the local control than for the original OGY control.

V. SUMMARY

Using two experimental systems, a driven pendulum and a driven bronze ribbon, we study the application of feedback control of chaos based on the OGY-control idea. As feedback control methods we use the original OGY method and the local-control method, explored in this paper. The original OGY method adjusts the control parameter once per driving period using knowledge about the stable and unstable eigendirections of an UPO in one Poincaré section. The local-control method in contrast adjusts the control parameter as often as needed for stabilization of the UPO using the singular value decomposition of the linearization, $A^n = D_{\mathbf{z}_F^n} \phi^{\Delta t}$, $\Delta t = T/N$, of the time local Poincaré mappings $\mathbf{P}^{(n,n+1)} = \phi^{\Delta t}_{|\Sigma_n}$ around an UPO $\mathbf{z}_F^n$. This approach has the advantage that one can circumvent possible complex eigenvalues of $D_{\mathbf{z}} \phi^{\Delta t}$ and allows to stabilize UPO's and also aperiodic chaotic orbits.

The main objective of our experiments is to compute all control vectors needed for both feedback control

schemes solely from the analysis of time series. To do this we apply the flow vector field analysis of Hübler to the pendulum to obtain a good global model for the system and thus very easily all relevant control quantities. For the bronze ribbon, on the other side, only linear fits in embedding space near recurrent points prove to be appropriate. Our analysis shows that both experimental systems are highly unstable having UPO's with comparatively large unstable eigenvalues, $|\lambda_u|$ being around 10, and in some Poincaré sections the UPO's exhibit stretching rates $\mu(\mathbf{z}_F^n, T) = \exp(\lambda_{eff}(\mathbf{z}_F^n, T)T)$ being of the order of 100 or more.

These large effective Lyapunov exponents cause severe problems regarding the determination of the linearizations $A_n^G = D_{\mathbf{z}_F^n}\mathbf{P}$ of the global Poincaré mapping of the OGY control and also regarding the performance of the original OGY-control itself.

Referring to the calculation of A_n^G we first determine A_n^G in each Poincaré section Σ_n from direct fits near recurrent points. A plot of the corresponding unstable (stable) eigenvalues λ_u^n (λ_s^n) versus n shows critical regions where λ_u^n (λ_s^n) fluctuate wildly violating the theoretical requirement that λ_u^n (λ_s^n) should be independent of n. This plot reveals that for highly unstable systems it is problematic to determine the linearized Poincaré mappings exclusively for a single section Σ_n. As a remedy we then calculate the A_n^G as a product of the local A^n. It turns out that the eigenvalues λ_u^n of these A_n^G which are independent of n by construction coincide with the plateaus of the λ_u^n determined from the direct fit. Furthermore, the analysis of the effective Lyapunov exponents of the new A_n^G reveals that the problems in the determination of A_n^G by a direct fit are caused by large $\lambda_{eff}(\mathbf{z}_F^n, T)$ in the corresponding Poincaré sections.

Thus having obtained good approximations of the OGY-control vectors we apply the original OGY control to both systems. Although we carefully avoid Poincaré sections with extremely high effective Lyapunov exponents we cannot stabilize the experiments monitoring the system in only one Poincaré section and then adjusting the control parameter only once per period. The effective Lyapunov exponents of our Poincaré sections are still too large to allow for a stabilization of the system in the presence of measurement noise. This statement is confirmed by the numerical experiment analyzing the effect of noise on the control.

Concerning the control quantities for the local control method only the determination of the dependence

$\mathbf{w}^n = \frac{\partial \mathbf{P}^{(n,n+1)}}{\partial p}$ of the local Poincaré mappings on the control parameter proves to be difficult using the shift of the fixed point $\mathbf{g}^n$ and the local mappings A^n determined from a fit. However, generally these quantities do not exhibit complicated dependence on the state space variables. For two-dimensional nonautonomous systems with the state space coordinates $(x, \dot{x}, \theta)$ of the equivalent autonomous system the vector $\mathbf{w}^n = (0, k\,\Delta t)$ can already be a good guess. Even noisy control vectors suffice to stabilize our experiments when the control is applied several times per period. For the bronze ribbon, however, one has to introduce an additional control rule to insure that the local control is not suspended when the calculated control vectors become too large. With this nearly continuous control we are then able to successfully control the bronze ribbon.

Finally, in our work we exploit two different approaches to calculate the control vectors necessary to obtain stabilization of unstable trajectories in experiment. One is to determine a global model of the dynamical system and the other one is to utilize fits of the dynamics near recurrent points. For the first approach all control vectors can be calculated straightforward even for an aperiodic motion. The second approach needs much more effort already for period-one orbits. These costs would increase immensely when one intended to control an aperiodic orbit. From this point of view efforts taken to achieve a global model describing the dynamics of the experiment are worthwhile. It is recommendable to check the chance of obtaining such a model before the alternative fit procedure is exploited. Regardless how the control values are determined our experiments show that for systems exhibiting large effective Lyapunov exponents a quasicontinuous approach to stabilize unstable trajectories proves to be necessary.

ACKNOWLEDGMENTS

[1] A. Hübler and E. Lüscher, Naturwissenschaften **76**, 67 (1989).

[2] E. Ott, C. Grebogi, and J.A. Yorke, Phys. Rev. Lett. **64**, 1196 (1990).

[3] T. Shinbrot, C. Grebogi, E. Ott, and J.A. Yorke, Nature **363**, 411 (1993).

[4] U. Dressler and G. Nitsche, Phys. Rev. Lett. **68**, 1 (1992).

[5] G. Nitsche and U. Dressler, Physica D **58**, 153 (1992).

[6] D. Auerbach, C. Grebogi, E. Ott, and J. A. Yorke, Phys. Rev. Lett. **69**, 3479 (1992).

[7] W.L. Ditto, S.N. Rauseo, and M.L. Spano, Phys. Rev. Lett. **65**, 3211 (1990).

[8] B. Hübinger, R. Doerner, and W. Martienssen, Z. Phys. B **90**, 103 (1993).

[9] C. Reyl, L. Flepp, R. Badii, and E. Brun, Phys. Rev. E **47**, 267 (1993).

[10] P. Parmananda, P. Sherard, R.W. Rollins, and H.D. Dewald, Phys. Rev. E **47**, R3003 (1993).

[11] V. Petrov, V. Gáspár, J. Masere, and K. Showalter, Nature **361**, 240 (1993).

[12] E.R. Hunt, Phys. Rev. Lett. **67**, 1953 (1991).

[13] R. Roy, Jr., T.W. Murphy, T.D. Maier, Z. Gills, and E.R. Hunt, Phys. Rev. Lett. **68**, 1259 (1992).

[14] J. Singer, Y.-Z. Wang, and H.H. Bau, Phys. Rev. Lett. **66**, 1123 (1991).

[15] K. Pyragas and A. Tamasevicius, Phys. Lett. A **180**, 99 (1993).

[16] S. Bielawski, M. Bouazzaoui, D. Derozier, and P. Glorieux, Phys. Rev. A **47**, 3276 (1993).

[17] S. Bielawski, D. Derozier, and P. Glorieux, Phys. Rev. A **47**, R2492 (1993).

[18] J. Cremers and A. Hübler, Z. Naturforsch. Teil A **42**, 797 (1987).

[19] R. Doerner, B. Hübinger, W. Martienssen, S. Grossmann, and S. Thomae, Chaos Solitons Fractals **1**, 553 (1991).

[20] F.J. Romeiras, C. Grebogi, E. Ott, and W.P. Dayawansa, Physica D **58**, 165 (1992).

[21] E. Ott, C. Grebogi, and J.A. Yorke, in *Chaos/XAOC Soviet-American Perspectives on Nonlinear Science*, edited by D. K. Campbell (AIP, New York, 1990), pp. 153–172.

[22] J. Warncke, M. Bauer, and W. Martienssen, Europhys. Lett. **25**, 323 (1994).

[23] F.C. Moon. *Chaotic Vibrations* (Wiley, New York, 1987), Vol. 1.

[24] D.P. Lathrop and E.J. Kostelich, Phys. Rev. A **40**, 4028 (1989).

[25] K. Pawelzik and H.G. Schuster, Phys. Rev. A **43**, 1808 (1991).

[26] R. Doerner, B. Hübinger, W. Martienssen, S. Grossmann, and S. Thomae (unpublished).

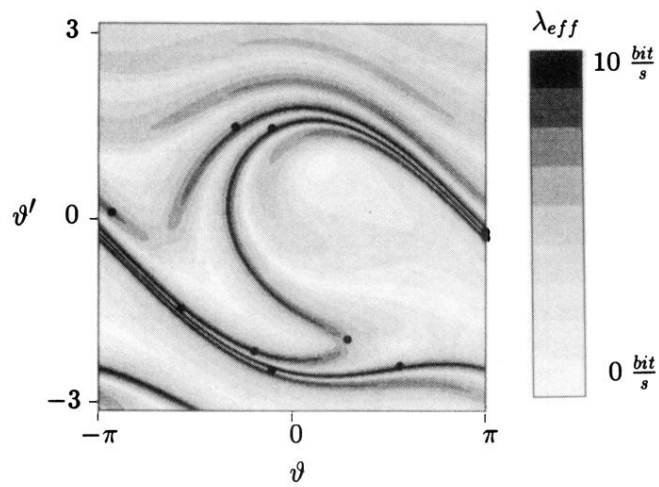[27] I.B. Schwartz and I. Triandaf, Phys. Rev. A **46**, 7439 (1992).

FIG. 13. Gray scale plot of the effective Lyapunov exponent $\lambda_{eff}(\vartheta, \vartheta', T)$ of the pendulum for the time T corresponding to one period of the driving in the Poincaré section $\psi = 0$. Dark zones indicate large exponents while bright zones correspond to low values of $\lambda_{eff}(\vartheta, \vartheta', T)$. The dots ($\bullet$) indicate ten period one UPO's in the section $\psi = 0$. Without exception they are located in regions with large effective Lyapunov exponents.

FIG. 3. The chaotic attractor of the driven pendulum in the Poincaré section $\psi = 0$. The driving period of the external torque is $T = 1.2$ s. The Hausdorff dimension for this attractor can be determined to $D_H \approx 2.8$.
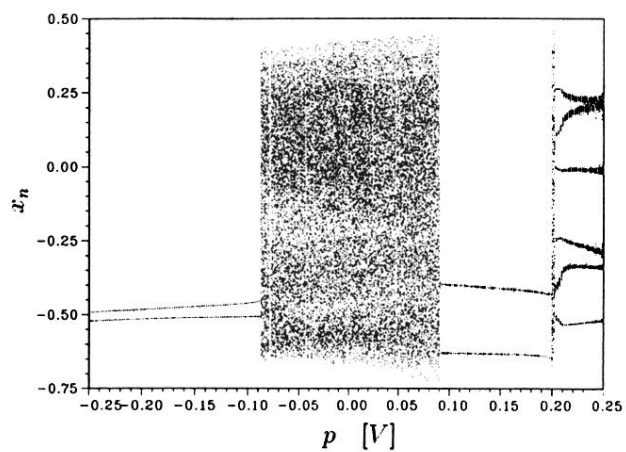
FIG. 5. Experimental bifurcation diagram of the bronze ribbon. Varying the offset voltage of the coils p as control parameter the stroboscopic measurements $x_n = x(n\,T)$ corresponding to $(\mathbf{z}_n)_1$ in the Poincaré section Σ_0 are plotted versus p.
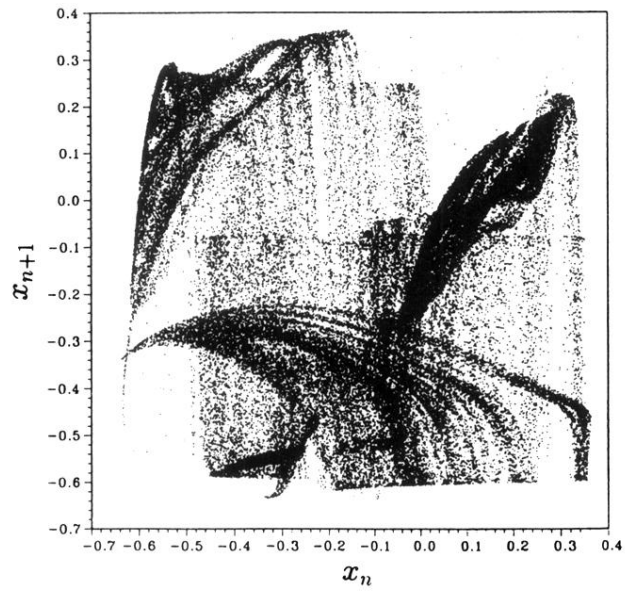
FIG. 6. First return map of the bronze ribbon for $p = 0$ V. $x_{n+1} = x[(n + 1)T]$ versus $x_n = x(nT)$ is plotted.
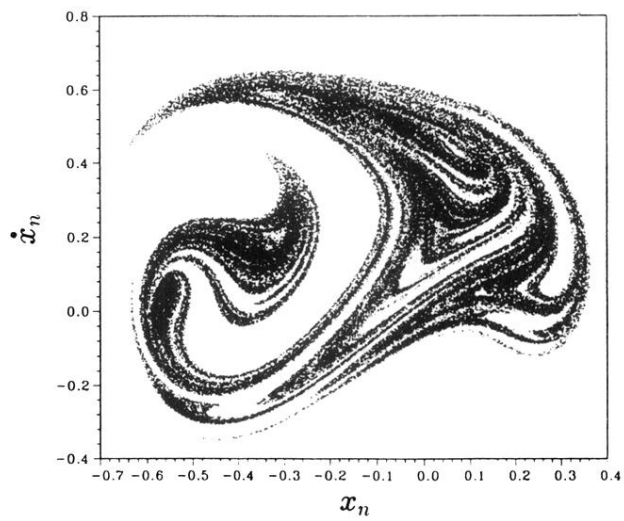
FIG. 7. Chaotic attractor for the bronze ribbon for $p = 0$ V. 100 000 points $\mathbf{z}_n = (x_n, \dot{x}_n)$ are shown in the Poincaré section Σ_0.